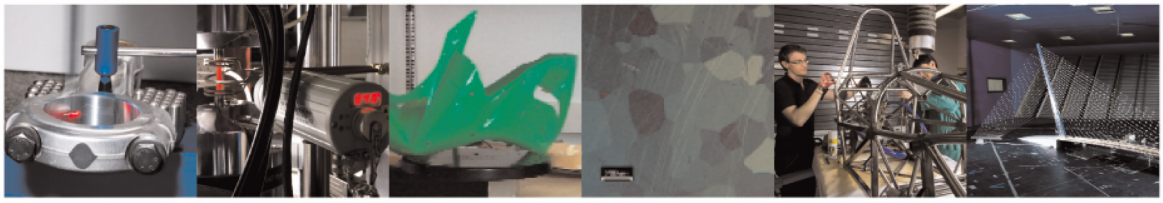

Mechanical and microstructural characterization of WC-Co consolidated by binder jetting additive manufacturing

Mariani, Marco; Goncharov, Ivan; Mariani, Davide; De Gaudenzi, Gian Pietro; Popovich, Anatoly ;Lecis, Nora; Vedani, Maurizio

This is a post-peer-review, pre-copyedit version of an article published in International Journal of Refractory Metals and Hard Materials. The final authenticated version is available online at: http://dx.doi.org/j.ijrmhm.2021.105639

Mechanical and microstructural characterization of WC-Co consolidated by binder jetting additive manufacturing

Marco Mariani[a], Ivan Goncharov*[a], Davide Mariani[a], Gian Pietro De Gaudenzi[b], Anatoly Popovich[c], Nora Lecis[a], Maurizio Vedani[a]

[a] Department of Mechanical Engineering, Politecnico di Milano, Milano 20156, Italy

[b] HI.Lab, FILMS S.pA. - OMCD Group, Anzola d'Ossola 28877, Italy

[c] Peter the Great St. Petersburg polytechnic University, St. Petersburg 195251, Russian Federation

corresponding author: ivan.goncharov@polimi.it

Abstract

A study was carried out to investigate the influence of the initial powder features on the microstructure, the phase composition, and on the mechanical properties of WC-12%Co samples produced by binder jetting and densified by sintering in vacuum at 1400°C and by sinter-HIPing. The initial powder consisted of a mixture of fine-grained and coarse-grained WC-based particles, and W_2C-based ones. The density of the printed samples was 97.4% and 99.3% after sintering and sinter-HIPing, respectively. Layer-oriented porosity was observed only in sintered samples. The microstructure of the samples consisted of a mixture of fine and coarse WC grains, which can be the result of the coalescence of grains from anomalous coarse grains in the powder particles. Vickers hardness and transverse rupture strength of sinter-HIPed samples are 1205 HV and 2257 MPa, respectively, which is coherent with the microstructural analysis and close to coarse-grained commercial products.

Graphical Abstract

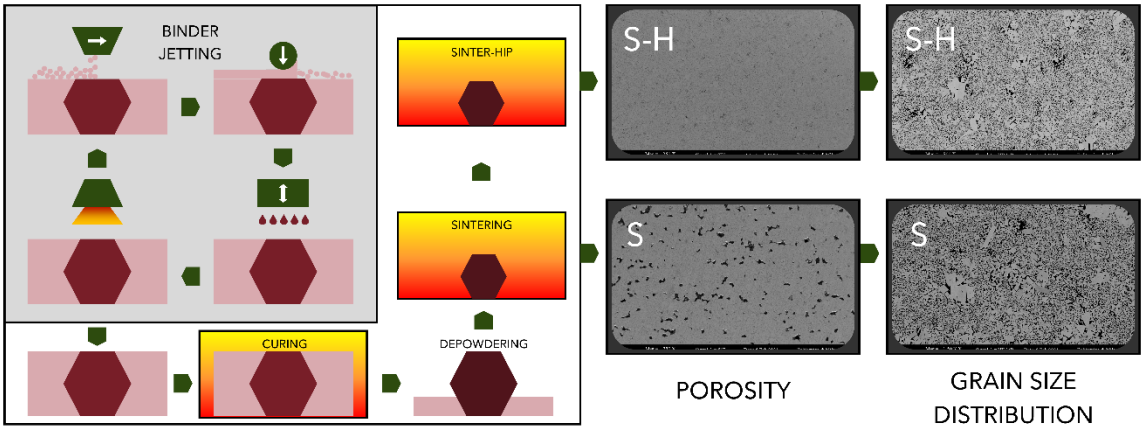

Keywords: cemented carbides, binder jetting; additive manufacturing; WC-Co; microstructure.

1. Introduction

Cemented carbides are a group of composite materials which consist of at least 2 phases – a hard transition metal carbide and a ductile metallic binder phase. They offer superior hardness, remarkable toughness, and wear resistance; hence they are widely used in application where all these properties are required, such as wear-resistant parts and milling tools. The most used cemented

carbide is WC-Co, followed by other systems as WC-TiCTaC-Co and WC-Ni. In addition to the effects of the chemical composition, the main properties of the composite such as hardness, strength, toughness, and wear resistance, depend also on the carbide grain size, its distribution and the binder content [1–6].

Traditional manufacturing methods are based on powder metallurgy principles of consolidating and sintering, including advanced techniques such as hot isostatic pressing (HIP) and spark plasma sintering (SPS) [7]. Besides, powder injection molding (PIM) and extrusion are also used [8–12]. In recent years, the need for complex shapes by application-oriented design has pushed toward the employment of additive manufacturing (AM) techniques to produce also this class of materials. Several studies have been reported focusing on different methods, such as laser powder bed fusion (LPBF) [13–27], laser engineered net shaping (LENS) [28,29], extrusion-based fused filament fabrication (FFF) [30,31], 3D gel-printing (3DGP) [32], and powder-based binder jetting additive manufacturing (BJAM) [33–36]. The main drawback of using the LPBF technique for the WC-Co system is the overheating induced by the laser that causes microcracks, decarburization of WC with the formation of undesirable η-phases, which are brittle complex carbides like W_3Co_3C, W_6Co_6C. Among all others, the BJ appears to be the most promising AM techniques to produce near-net-shape WC-based parts because the printing process of the green part with the organic binder occurs at low temperature, while densification by sintering or sinter-HIPing are performed separately, at the solid stage, similarly to the traditional and well-developed manufacturing technologies.

There are reports on the use of binder jetting additive manufacturing for the WC-Co system. Enneti et al. [36–38] used pre-alloyed WC-Co powder with sintering and sinter-HIP as consolidation techniques. In contrast, Cramer et al. [33,39–41] used pure WC powder to produce a green model, and then they infiltrated it with a liquid Co-based mixture. From these few reports available in the open literature, limited description is provided about the microstructural evolution and the mechanical behaviour of WC-based materials during the printing phase and in the subsequent consolidation stage.

In this study, we investigated the influence of the initial powder features on the microstructure, the phase composition, and on the mechanical and magnetic properties of WC-Co samples produced by BJ and densified either by sintering or by sinter-HIPing.

2. Materials and Methods

2.1. Materials

For this study, the powder employed was a WC-12Co (wt.%), provided by Global Tungsten & Powders Corp. (US) (AM WC702). The powder size lies in the range 5-20 μm (d_{10}-d_{90}) and the apparent density is about 4-8 g cm^{-3}, according to the product datasheet. The binder employed in the printing process was provided by ExOne Inc. and is a commercial water-based product (code: BA-005).

2.2. Powder Characterization

The powder surface and sections of powder particles after mounting, polishing and etching were visually analysed via a ZEISS SIGMA 500 field emission-scanning electron microscopy (FE-SEM), which also provided chemical composition measurements by energy dispersion X-ray detection

(EDX). SEM images were inspected and analysed by ImageJ software to determine the grain size and the powder size distribution [42].

The morphological features of the powders were determined by a Malvern Morphology 4 granulometer (ASTM E2651-19). The analysis allowed to calculate the number-based relative and cumulative frequency distributions and to evaluate the particles circularity, calculated as the ratio of the circumscribed circle on the actual particle section perimeter.

The crystal structure and phase composition of the powder was studied by Smartlab II Rigaku X-ray diffractometer. The measurement was performed with a Cu-Kα radiation (λ = 1.5406 Å) at a scanning rate of 1° min^{-1}, from 10° to 100° and with a step size of 0.02°.

2.3. Printing Process and Thermal Treatments

The samples were produced with an Innovent+ 3D printer by ExOne Inc. The printing parameters are given in Table 1 and have been selected after preliminary parameter optimization. A small layer thickness (50 μm) was chosen to assure an optimal geometrical accuracy and proper powder packing, and a 60% binder saturation to allow safe handling of the green bodies and minimize the amount of organic residual throughout the process [38]. This was of paramount importance given the detrimental effect of excess carbon resulting from binder decomposition on the microstructure, thus on the mechanical performance of the sintered components.

Table 1 BJ printing parameters.

Layer thickness	50 μm
Binder saturation	60%
Drying time	12 s
Recoat speed	300 mm/s

After the printing, the curing was performed at 180 °C for 6 hours in air to eliminate the binder solvents and solidify the polymeric network, as required for the safe extraction of the green bodies from the unbound powder. These samples (i.e. the green bodies) were then debinded/pre-sintered at 500 °C for 4 hours in nitrogen atmosphere and finally sintered at 1400 °C under vacuum. Further densification by HIP under a 35 bar pressure was performed for 20 minutes at 1400 °C. IN the following, we will refer to sintered samples using the letter “S”, and to sintered and HIPed ones with “SH”.

2.4. Microstructural and Mechanical Characterization

The efficacy of the thermal treatments was monitored by density measurements at each step of the process. Green densities were estimated by a simplified geometrical method based on the gross volume and weight of samples, due to large extent of porosity. Archimede’s method was applied to S and SH specimens (ASTM B311 – 17). The theoretical density of WC – 12 wt.% Co was considered to be 14.29 g cm^{-3}. Linear shrinkage was calculated by measuring S and SH 3-point bending test specimens with a digital caliper along the X (Roller Axis), Y (Printhead Axis) and Z (build direction). The microstructure was studied by optical and scanning electron microscopy on polished transverse and longitudinal sections (ASTM E3 – 11), and on samples etched by Murakami’s reagent (ASTM

E407 - 7), to determine the grain and pore size distributions and the presence of defects such as carbon segregation and formation of η-phases. The samples were characterized also by XRD, with the parameters described in the paragraph 2.3.

Eight SH specimens were mechanically characterized by Vickers hardness (HV) measurement with an applied load of 10 kgf for 15 seconds on polished surfaces (ASTM C1327-14) and by 3-point bending test on grounded samples with a constant load displacement rate of 0.5 mm min^{-1} (ISO 3327) to assess the transverse rupture strength (TRS). TRS was calculated as follows in Eq. 1:

$$TRS = 3\,k\,F\,l\,/\,(2\,w\,h^2) \qquad (1)$$

where k = 1.02 is the chamfer correction value, F is the force applied, l is the span length, and w, h are the specimen width and height, respectively.

3. Results and Discussion

3.1. Powder Characterization

SEM images of the polished sections of particles revealed that the powder employed was a mixture of three different particle types, as observed in Figure 1A and in Figure 2. Specifically, it was possible to identify particles with a uniform distribution of fine WC grains (Figure 1B), with maximum size of about 3-4 μm, in a limited amount of cobalt matrix. In addition, particles with coarse WC grains size up to 10 μm were detected with noticeable intragranular porosity (indicated by the circle in Figure 1C), which can be the result of coalescence of fine grains during the powder production process, and other slightly smaller particles with finer W_2C columnar grains (Figure 1D). It is worth noticing that these latter particles seem to be often affected by internal porosity which could prevent full densification during post-processing, particularly during pressureless sintering, in addition to represent a dangerous site for fracture nucleation. The presence of W_2C must be considered when planning the post-processing, as it requires to correct the carbon balance to avoid the formation of detrimental phases in the final microstructure. A solution could be a carbon-correction cycle with methane during the heating ramp, as done by Enneti et al. [36]. The formation of coarse-grained particles can presumably be explained by the occurrence of WC recrystallization during melting and subsequent cooling of the powder in a thermal plasma spheroidization process.

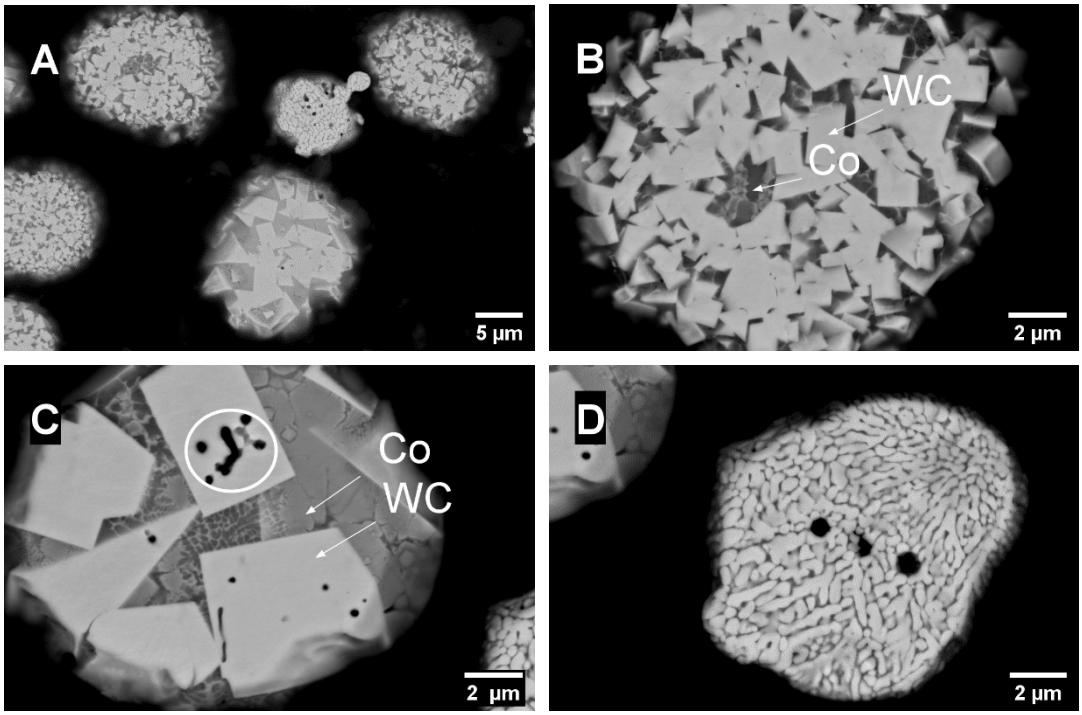

Figure 1 SEM micrographs of the polished sections of (A) WC-Co powder, (B) a particle with fine WC grains in Co matrix, (C) a particle with coarse WC grains in Co matrix, and (D) a particle with W_2C columnar grains.

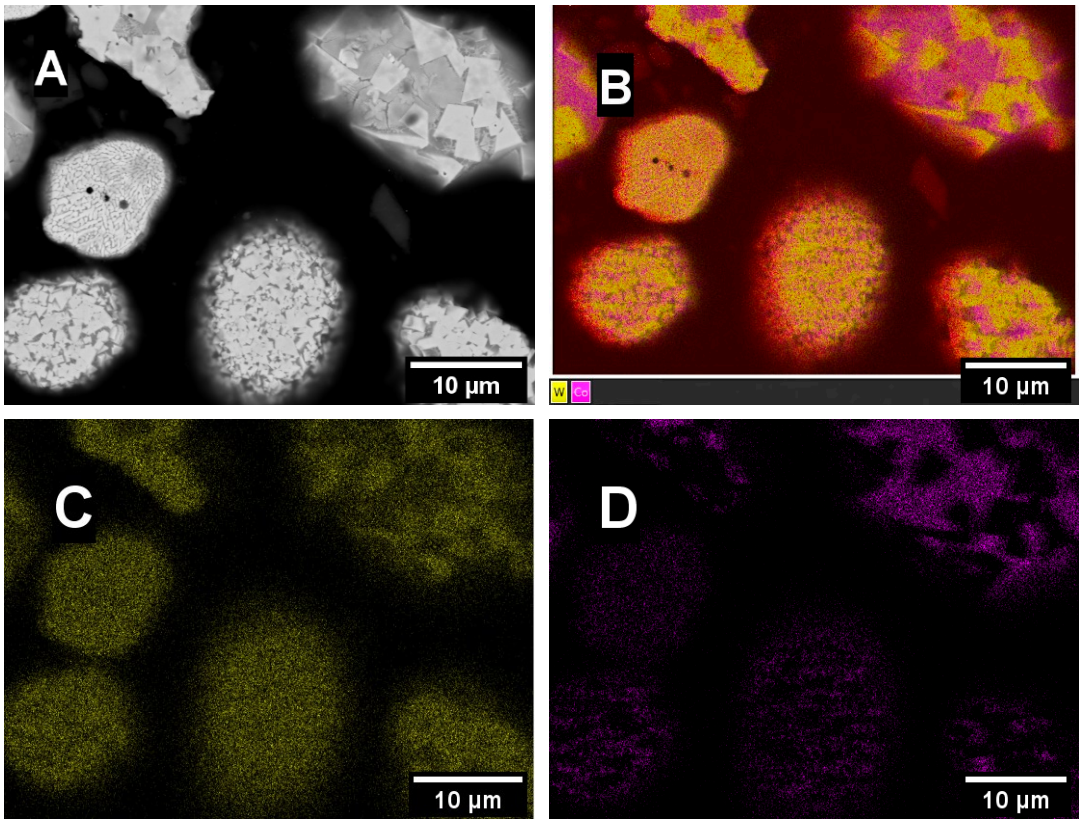

Figure 2 Elemental mapping of different particles of the WC-12Co (wt.%) powder investigated: (A) SEM micrograph; (B) Combined map; (C) Map of W; (D) Map of Co.

The X-ray diffractometry spectrum given in Figure 3 confirms the nature of the different phases identified in the three particle types by SEM-EDX. WC is the main phase in terms of overall amount, however peaks of the W_2C can be identified, as well as those generated by the Cobalt matrix.

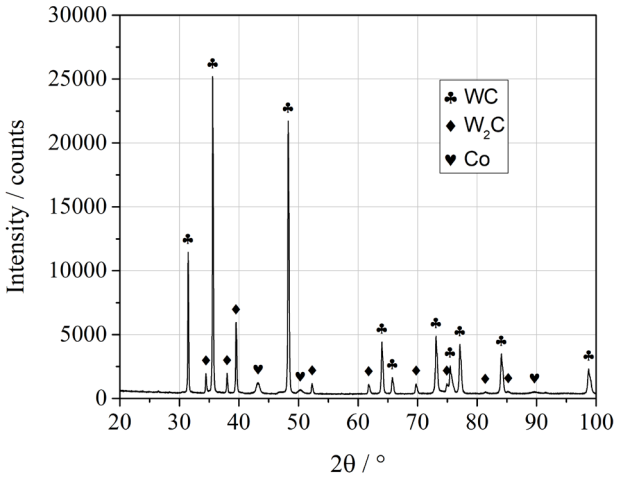

Figure 3 XRD spectrum of the as-received WC-12Co powder.

Granulometric measurements presented in Figure 4 apparently show the presence of a bimodal population of particles, whose size-distribution bells are partially overlapped. Indeed, the overall value of d_{50} from granulometric measurement was 3.5 μm (Figure 4A), which is significantly different from the nominal values of 15 – 30 μm given by the supplier and the average value of 16.6 μm measured by ImageJ. The difference is most likely due to the presence of fine spherical particles in the supplied material resulting from evaporation and condensation of the powder particles during plasma spheroidization. These particles are detected by the granulometer, but they are difficult to be visually analysed. Some examples of the small-size fraction of particles are also highlighted in Figure 5.

Although larger granules are fundamental to obtain a proper powder flowability and spreadability during the printing phase, the presence of smaller ones should not be neglected. Indeed, they tend to increase the packing density of the powder bed by filling the voids between larger particles and they affect the sintering process since solubility, diffusivity and grain growth are also related to the particles radius [6].

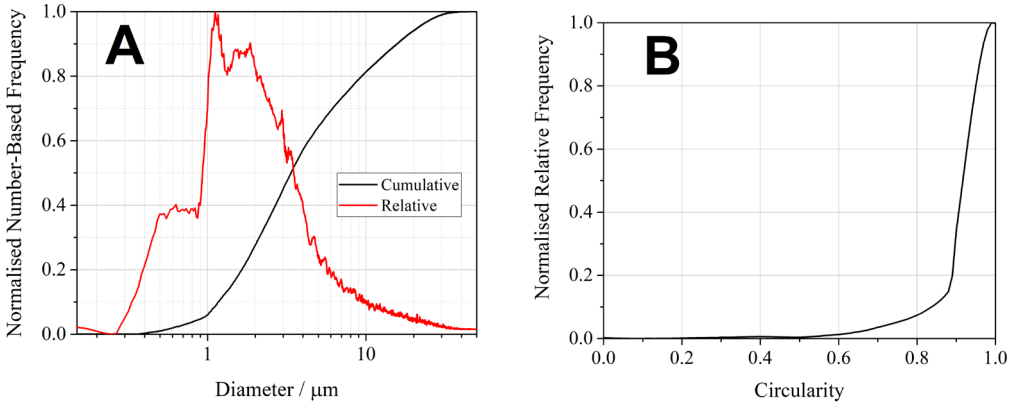

Figure 4 Granulometric analysis of the powder particles: (A) Cumulative and relative frequency distributions (number-based); (B) Circularity measurement curve.

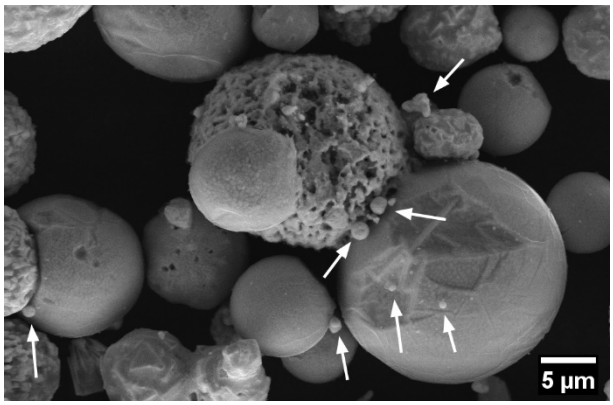

Figure 5 SEM image of the initial powder with fine particles.

3.2. Microstructural Characterization

The printing process revealed to be highly repeatable and reliable, as demonstrated by the low standard deviation of the green density obtained from measuring 15 samples (Table 2). The drastic increase of the density after sintering and sinter-HIP processes is accompanied by the change of geometrical dimensions, resulting in an approximate shrinkage for sintering of 21% by X-axis, 23% by Y-axis, 20% by Z-axis, for sinter-HIP of 23% for X-axis, 26% for Y-axis, 23% for Z-axis.

Table 2 Average relative density (%) values at the green (G), sintering (S) and sinter-HIP (SH) stages.

Relative Density / %		
G	*S*	*SH*
47.3 ± 0.6	97.4 ± 0.1	99.3 ± 0.3

The microstructure of the samples after pressureless sintering is shown in Figure 6. A noticeable number of pores is observed on transversal sections along the powder layer direction. The average pore size is about 18 µm, which is coherent with the average particle size. The volume occupied by the densified material consists of two areas: the main one features a fine carbide-cobalt mixture, in which the WC grains size is about 1-3 µm, in the remaining area coarse WC grains are observed, as

highlighted in Figure 6B. The coarse WC grain size can be up to more than 30 μm. In accordance with the EDX analyses, there are also carbon-enriched dendritic zones, which can be the proof of the presence of residual carbon from the organic binder that could not be totally removed during the debinding stage due to the lack of an oxidizing atmosphere during thermal treatments. The excess carbon contributed to the carburization of the W_2C grains present in the powder. However, it could also produce a graphitic phase which is detrimental to the performances of the components.

The grains size and their morphology are similar to the dual distribution observed in the powder particles. The coalescence of grains and their further growth (by Ostwald ripening) may presumably start from the anomalous coarse grains in the powder particles, while the fine-grained mixture is formed after sintering of regular powder particles and it experienced a slower increase in size (Figure 6C). Inside the coarse-grained zones are also detected regions enriched with cobalt, allocated along the boundaries of WC grains (Figure 7).

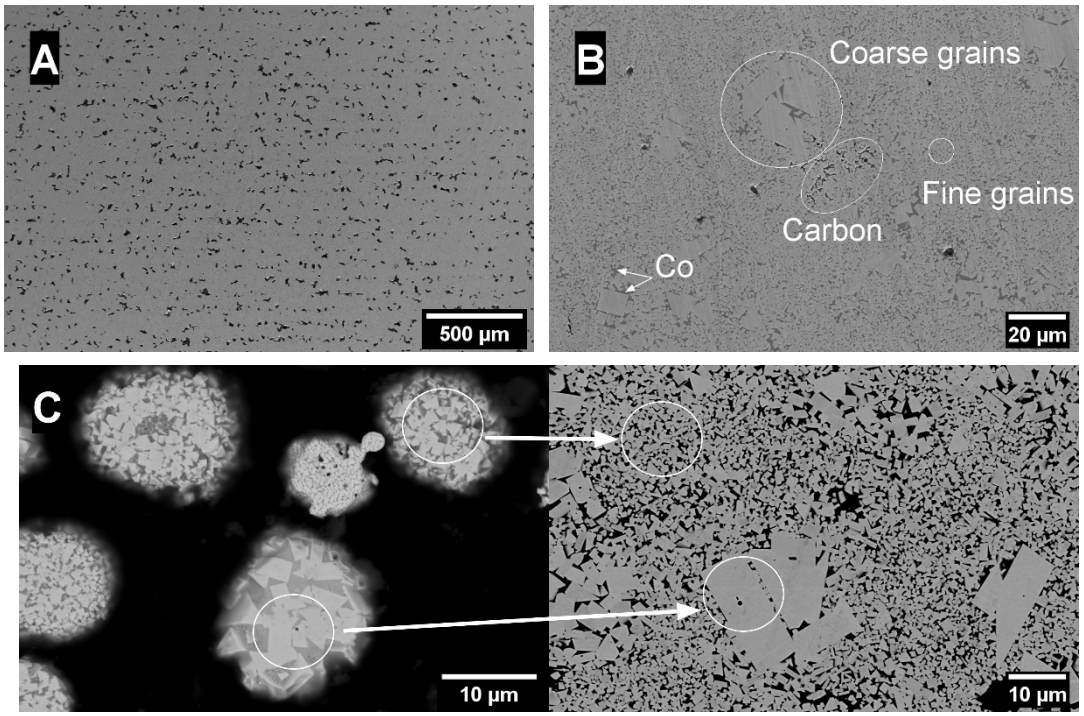

Figure 6 SEM images of WC-12Co sintered sample in secondary electrons mode: (A) transverse section of the sample; (B) microstructural details (x1500); (C) the conjectured evolution of microstructure from the powder to the bulk sample.

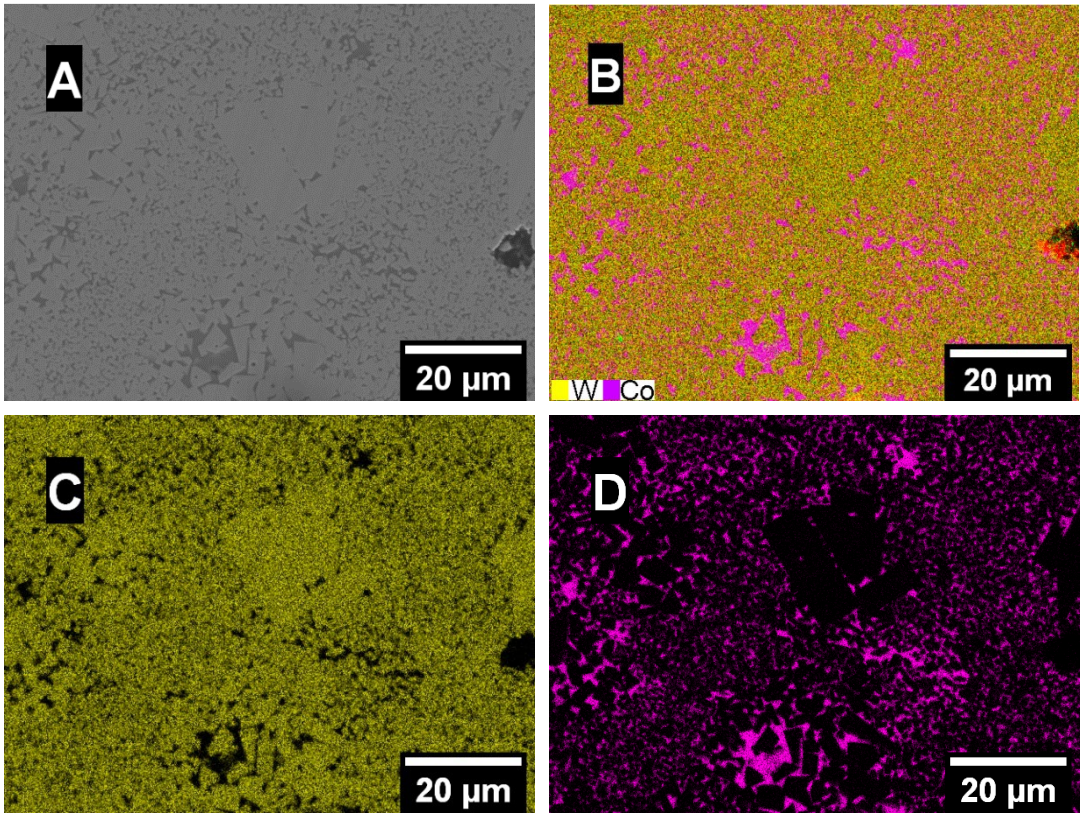

Figure 7 Elemental mapping of WC-12Co sample after sintering (A) SEM image; (B) Combined map; (C) Map of W; (D) Map of Co.

The microstructure of the samples after sinter-HIP is shown in Figure 8. The transverse section appears to be much less porous in comparison to the sintered sample, coherently with the increase of relative density measured (Table 2). The average pore size is about 1.5 µm, thus it reduced to a tenth of that found in the sintered samples. At higher magnification (Figure 8B), also in this case a distinction between the two zones of WC-Co mixtures can be noticed: the sinter-HIP treatment was able to densify the samples by closing the internal porosity, but it did not produce significant changes in the carbides. The coarser grains size approaches about 40 µm, while the carbides in fine-grained mixture are in the 1-3 µm size range. The overall WC grain size distribution is summarized in Figure 9, resulting in an average value of 8 µm. From the distribution plot, the long right tail of the curve due to the above coarse grains should be noted. Besides the amount and size of pores, the microstructure appears to be similar to the vacuum sintered sample. There is a noticeable amount of spherical-shaped submicron pores inside of coarse WC grains (Figure 8 C,D), which may either be transferred from anomalous powder particles.

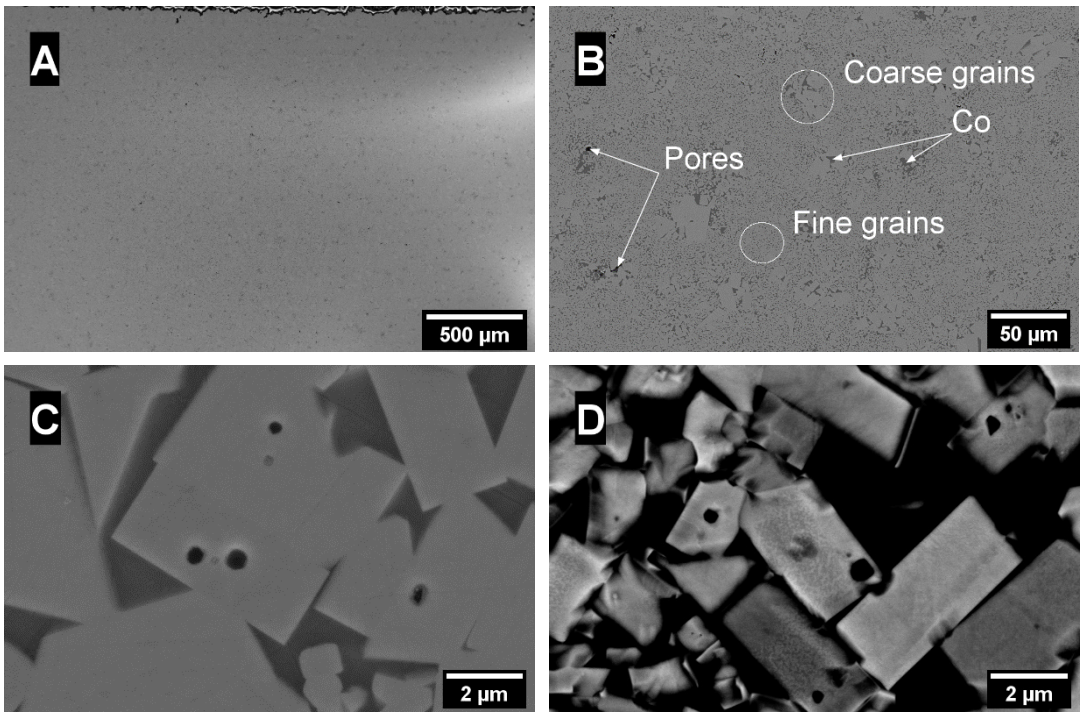

Figure 8 SEM images of sample after sinter-HIP: (A) transverse section of the sample; (B) microstructural details, (C) and (D) Coarse WC grains with internal porosity polished and etched, respectively.

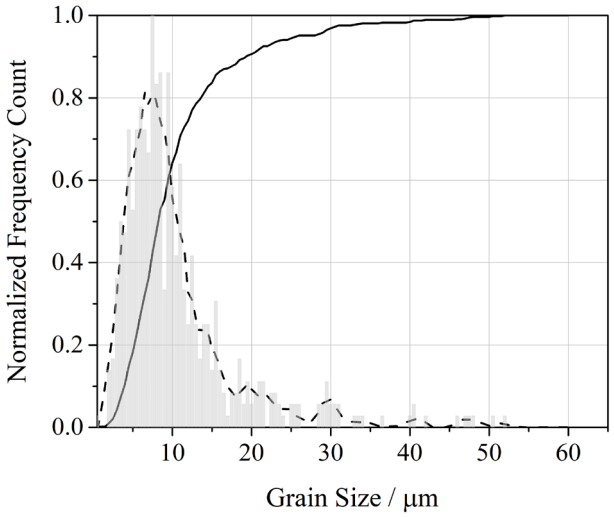

Figure 9 Cumulative and relative frequency curves of the WC grain size distribution of the sample after sinter-HIP

The XRD patterns of the sintered and sinter-HIPed samples given in Figure 10 show that the W_2C diffraction pattern is not detected anymore (compare with Figure 3) in both cases, suggesting that this phase was successfully carburized throughout the process likely thanks to the excess carbon introduced by the organic binder. Both samples also display very weak signals coming from the limited amount of graphitic phase, that can be spotted in specific locations of the microstructure.

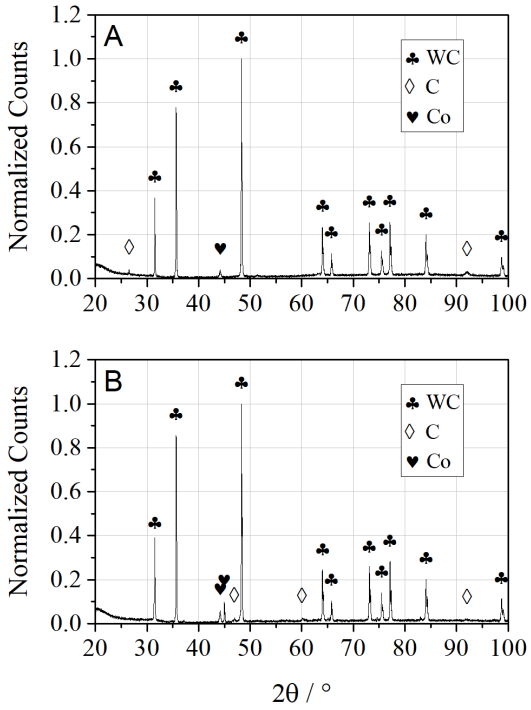

Figure 10 XRD spectra of the samples after sintering (A) and sinter-HIP (B).

3.3. Mechanical Characterization

To evaluate the achievable mechanical performance, 3-point bending test was performed on the SH sample that showed the best density among the conditions here investigated. TRS and hardness of the samples after sinter-HIPing (Table 3) lies within the typical range for cemented carbides and approximates the performance of traditionally manufactured WC-Co cemented carbide with coarse (2.5-6 μm) WC grain size (Figure 11) [43,44], which well correlates with the results of our microstructure analysis. The presence of large grains is crucial in determining the overall performance of the printed components, even though most of the material features a finer microstructure. The absence of relevant porosity is equally important as it would otherwise compromise the mechanical performance and act as a preferential site for crack nucleation [45].

The hardness value measured is comparable with the results obtained by BJ of pre-alloyed powders with the same amount of cobalt [36] and superior to binder jetted-WC infiltrated components [33] and 3D gel-printed samples [32], which both featured a larger amount of Co.

Table 3 Results of Vickers hardness and 3-point bending test measurements of SH samples.

Vickers Hardness	**Transverse rupture strength**
HV_{10}	MPa
1205 ± 12	2257 ± 28

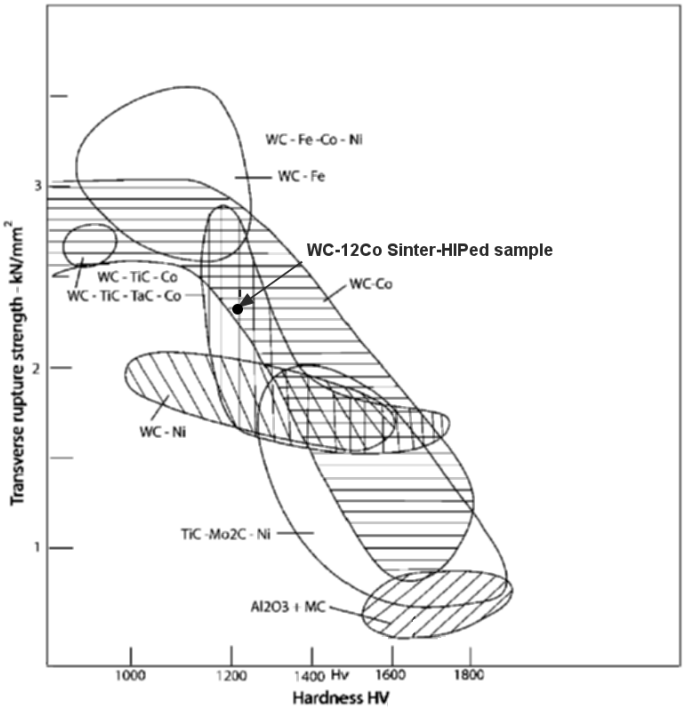

Figure 11 Relationship between the TRS and hardness of WC-based materials. Marked point corresponds to SH sample [44].

4. Conclusions

A study was carried out to analyse the microstructure and the properties of WC-12Co (wt.%) powder and bulk samples produced by binder jetting additive manufacturing, with subsequent sintering and sinter-HIP treatments.

According to the FE-SEM analysis, elemental mapping, and X-ray diffractometry, there are three main types of particles in the powder mixture: particles with fine and uniformly distributed WC grains; particles with coarse WC grains (up to 10 μm) and a noticeable amount of inner porosity; and W_2C-based spherical particles. The presence of coarse-grained and W_2C-based particles can presumably be explained by the overheating during the spheroidization process, leading to recrystallization and decarburization. The excessive heat input is also indirectly indicated by the presence of submicron spherical particles, typical for plasma spheroidization, which are the result of an evaporation-condensation process.

After sintering and sinter-HIP, the obtained density was 97.4% and 99.3%, respectively. The microstructure consisted of two areas – the fine-grained and the coarse-grained. The coalescence of grains and their further growth may presumably start from the anomalous coarse grains observed in the powder particles, while the fine-grained mixture is formed after sintering of regular powder particles, and it experiences a slower growth. There was evidence of the presence of excessive carbon after pressureless sintering, that was likely the result of incomplete organic binder burnout. There were no signs of W_2C phase, suggesting that a carburization process occurred. The sinter-HIP treatment was able to more effectively densify the samples by closing most of the internal porosity. However, there was a noticeable amount of spherical-shaped submicron pores inside of coarse WC grains, which may either have been transferred from anomalous powder particles or has occurred as the result of the applied pressure and closure of pores between the WC grans during sinter-HIP.

Transverse rupture strength and hardness of the samples after sinter-HIP lies in the typical range for cemented carbides and approximates the traditionally manufactured WC-Co cemented carbide with coarse (2.5-6 μm) and extra coarse (>6 μm) WC grain size, which well correlates with the results of microstructure analysis. This confirms the suitability of binder jetting 3D printing for the production of commercial-grade components, although a particular focus on initial powder and microstructural evolution is needed to obtain excellent performances.

Acknowledgments

Authors would like to acknowledge the "Functional Sintered Materials (Funtasma)" Interdepartmental Laboratory of Politecnico di Milano, where this research activity was developed. Support by the Italian Ministry for Education, University and Research through the project Department of Excellence LIS4.0 (Integrated Laboratory for Lightweight e Smart Structures) is also acknowledged.

Finally, authors would like to acknowledge the support given by Sandra Tedeschi for the preparation and analysis of the sintered and sinter-HIP samples at HI.Lab.

Funding

This research did not receive any specific grant from funding agencies in the public, commercial, or not-for-profit sectors.

References

1. Ryu, T.; Sohn, H.Y.; Hwang, K.S.; Fang, Z.Z. Plasma synthesis of tungsten carbide and cobalt nanocomposite powder. *J. Alloys Compd.* **2009**, *481*, 274–277, doi:10.1016/j.jallcom.2009.03.134.
2. Lay, S.; Allibert, C.H.; Christensen, M.; Wahnström, G. Morphology of WC grains in WC-Co alloys. *Mater. Sci. Eng. A* **2008**, *486*, 253–261, doi:10.1016/j.msea.2007.09.019.
3. Marshall, J.M.; Kusoffsky, A. Binder phase structure in fine and coarse WC-Co hard metals with Cr and v carbide additions. *Int. J. Refract. Met. Hard Mater.* **2013**, *40*, 27–35, doi:10.1016/j.ijrmhm.2013.04.001.
4. Petersson, A.; Ågren, J. Sintering shrinkage of WC-Co materials with different compositions. In Proceedings of the International Journal of Refractory Metals and Hard Materials; Elsevier, 2005; Vol. 23, pp. 258–266.
5. Gille, G.; Szesny, B.; Dreyer, K.; van den Berg, H.; Schmidt, J.; Gestrich, T.; Leitner, G. Submicron and ultrafine grained hardmetals for microdrills and metal cutting inserts. *Int. J. Refract. Met. Hard Mater.* **2002**, *20*, 3–22, doi:10.1016/S0263-4368(01)00066-X.
6. García, J.; Collado Ciprés, V.; Blomqvist, A.; Kaplan, B. Cemented carbide microstructures: a review. *Int. J. Refract. Met. Hard Mater.* **2019**, *80*, 40–68, doi:10.1016/j.ijrmhm.2018.12.004.
7. Upadhyaya, G.S. Cemented tungsten carbides. *Mater. Des.* **2001**, *22*, 411–412, doi:10.1016/S0261-3069(00)00091-1.
8. Youseffi, M.; Menzies, I.A. Injection Moulding of WC–6Co Powder Using Two New Binder Systems Based on Montanester Waxes and Water Soluble Gelling Polymers. *Powder Metall.* **1997**, *40*, 62–65, doi:10.1179/pom.1997.40.1.62.

9. Lin, D.; Xu, J.; Shan, Z.; Chung, S.T.; Park, S.J. Fabrication of WC-Co cutting tool by powder injection molding. *Int. J. Precis. Eng. Manuf.* **2015**, *16*, 1435–1439, doi:10.1007/s12541-015-0189-8.
10. Li, T.; Li, Q.; Fuh, J.Y.H.; Yu, P.C.; Lu, L. Two-material powder injection molding of functionally graded WC–Co components. *Int. J. Refract. Met. Hard Mater.* **2009**, *27*, 95–100, doi:10.1016/j.ijrmhm.2008.04.005.
11. Zhou, J.; Huang, B.; Wu, E. Extrusion moulding of hard-metal powder using a novel binder system. *J. Mater. Process. Technol.* **2003**, *137*, 21–24, doi:10.1016/S0924-0136(02)01058-0.
12. Ferstl, H.; Barbist, R.; Rough, S.L.; Wilson, D.I. Influence of visco-elastic binder properties on ram extrusion of a hardmetal paste. *J. Mater. Sci.* **2012**, *47*, 6835–6848, doi:10.1007/s10853-012-6627-4.
13. M., P. Additive Manufacturing of Tungsten Carbide Hardmetal Parts by Selective Laser Melting (SLM), Selective Laser Sintering (SLS) and Binder Jet 3D Printing (BJ3DP) Techniques. *Lasers Manuf. Mater. Process.* **2020**, *7*, 338–371, doi:10.1007/s40516-020-00124-0.
14. Domashenkov, A.; Borbély, A.; Smurov, I. Structural modifications of WC/Co nanophased and conventional powders processed by selective laser melting. *Mater. Manuf. Process.* **2017**, *32*, 93–100, doi:10.1080/10426914.2016.1176195.
15. Kyogoku, H.; Uemori, T.; Ikuta, A.; Yoshikawa, K.; Ohmori, H. Direct Selective Laser Sintering of WC-Co Cemented Carbide by Premixing of Additives. In Proceedings of the ASME/ISCIE 2012 International Symposium on Flexible Automation; American Society of Mechanical Engineers, 2012; pp. 465–468.
16. Ghosh, S.K.; Das, A.K.; Saha, P. Selective Laser Sintering: A Case Study of Tungsten Carbide and Cobalt Powder Sintering by Pulsed Nd:YAG Laser. In; Springer, New Delhi, 2015; pp. 441–459.
17. Yegyan Kumar, A.; Bai, Y.; Eklund, A.; Williams, C.B. The effects of Hot Isostatic Pressing on parts fabricated by binder jetting additive manufacturing. *Addit. Manuf.* **2018**, *24*, 115–124, doi:10.1016/j.addma.2018.09.021.
18. Wang, X.C.; Laoui, T.; Bonse, J.; Kruth, J.P.; Lauwers, B.; Froyen, L. Direct Selective Laser Sintering of Hard Metal Powders: Experimental Study and Simulation. *Int. J. Adv. Manuf. Technol.* **2002**, *19*, 351–357, doi:10.1007/s001700200024.
19. GU, D.; SHEN, Y.; DAI, P.; YANG, M. Microstructure and property of sub-micro WC-10 %Co particulate reinforced Cu matrix composites prepared by selective laser sintering. *Trans. Nonferrous Met. Soc. China* **2006**, *16*, 357–362, doi:10.1016/S1003-6326(06)60061-7.
20. Uhlmann, E.; Bergmann, A.; Gridin, W. Investigation on Additive Manufacturing of Tungsten Carbide-cobalt by Selective Laser Melting. *Procedia CIRP* **2015**, *35*, 8–15, doi:10.1016/j.procir.2015.08.060.
21. Gu, D.; Meiners, W. Microstructure characteristics and formation mechanisms of in situ WC cemented carbide based hardmetals prepared by Selective Laser Melting. *Mater. Sci. Eng. A* **2010**, *527*, 7585–7592, doi:10.1016/j.msea.2010.08.075.
22. Campanelli, S.L.; Contuzzi, N.; Posa, P.; Angelastro, A. Printability and Microstructure of Selective Laser Melting of WC/Co/Cr Powder. *Materials (Basel).* **2019**, *12*, 2397,

doi:10.3390/ma12152397.

23. Khmyrov, R.S.; Safronov, V.A.; Gusarov, A.V. Obtaining Crack-free WC-Co Alloys by Selective Laser Melting. *Phys. Procedia* **2016**, *83*, 874–881, doi:10.1016/j.phpro.2016.08.091.
24. Grigoriev, S.; Tarasova, T.; Gusarov, A.; Khmyrov, R.; Egorov, S. Possibilities of Manufacturing Products from Cermet Compositions Using Nanoscale Powders by Additive Manufacturing Methods. *Materials (Basel).* **2019**, *12*, 3425, doi:10.3390/ma12203425.
25. Chen, J.; Huang, M.; Fang, Z.Z.; Koopman, M.; Liu, W.; Deng, X.; Zhao, Z.; Chen, S.; Wu, S.; Liu, J.; et al. Microstructure analysis of high density WC-Co composite prepared by one step selective laser melting. *Int. J. Refract. Met. Hard Mater.* **2019**, *84*, 104980, doi:10.1016/j.ijrmhm.2019.104980.
26. Ku, N.; Pittari, J.J.; Kilczewski, S.; Kudzal, A. Additive Manufacturing of Cemented Tungsten Carbide with a Cobalt-Free Alloy Binder by Selective Laser Melting for High-Hardness Applications. *JOM* **2019**, *71*, 1535–1542, doi:10.1007/s11837-019-03366-2.
27. Fernandes, C.M.; Cavaleiro, A.; Gestel, C.V.; Jhabvala, J.; Boillat, E.; Vieira, M.T.; Senos, A.M.R. Microstructural characterization of WC-AISI304 composites obtained by selective laser sintering. *Microsc. Microanal.* **2015**, *21*, 104–105, doi:10.1017/S1431927614014226.
28. Xiong, Y.; Smugeresky, J.E.; Ajdelsztajn, L.; Schoenung, J.M. Fabrication of WC–Co cermets by laser engineered net shaping. *Mater. Sci. Eng. A* **2008**, *493*, 261–266, doi:10.1016/j.msea.2007.05.125.
29. Davoren, B.; Sacks, N.; Theron, M. Laser engineered net shaping of WC-9.2wt%Ni alloys: A feasibility study. *Int. J. Refract. Met. Hard Mater.* **2020**, *86*, 105136, doi:10.1016/j.ijrmhm.2019.105136.
30. Lengauer, W.; Duretek, I.; Fürst, M.; Schwarz, V.; Gonzalez-Gutierrez, J.; Schuschnigg, S.; Kukla, C.; Kitzmantel, M.; Neubauer, E.; Lieberwirth, C.; et al. Fabrication and properties of extrusion-based 3D-printed hardmetal and cermet components. *Int. J. Refract. Met. Hard Mater.* **2019**, *82*, 141–149, doi:10.1016/j.ijrmhm.2019.04.011.
31. Kitzmantel, M.; Lengauer, W.; Duretek, I.; Schwarz, V.; Kukla, C.; Lieberwirth, C.; Morrison, V.; Wilfinger, T.; Neubauer, E.; Kitzmante, M.; et al. Potential of Extrusion Based 3D-printed Hardmetal and Cermet Parts. *2018 World Congr. Powder Metall.* **2018**, 938–945.
32. Zhang, X.; Guo, Z.; Chen, C.; Yang, W. Additive manufacturing of WC-20Co components by 3D gel-printing. *Int. J. Refract. Met. Hard Mater.* **2018**, *70*, 215–223, doi:10.1016/j.ijrmhm.2017.10.005.
33. Cramer, C.L.; Aguirre, T.G.; Wieber, N.R.; Lowden, R.A.; Trofimov, A.A.; Wang, H.; Yan, J.; Paranthaman, M.P.; Elliott, A.M. Binder jet printed WC infiltrated with pre-made melt of WC and Co. *Int. J. Refract. Met. Hard Mater.* **2020**, *87*, 105137, doi:10.1016/j.ijrmhm.2019.105137.
34. Mudanyi, R.K.; Cramer, C.L.; Elliott, A.M.; Unocic, K.A.; Guo, Q.; Kumar, D. W-ZrC composites prepared by reactive melt infiltration of Zr2Cu alloy into binder jet 3D printed WC preforms. *Int. J. Refract. Met. Hard Mater.* **2021**, *94*, 105411, doi:10.1016/j.ijrmhm.2020.105411.
35. Arnold, J.M.; Cramer, C.L.; Elliott, A.M.; Nandwana, P.; Babu, S.S. Microstructure evolution during near-net-shape fabrication of NixAly-TiC cermets through binder jet additive manufacturing and pressureless melt infiltration. *Int. J. Refract. Met. Hard Mater.* **2019**, *84*,

104985, doi:10.1016/j.ijrmhm.2019.104985.
36. Enneti, R.K.; Prough, K.C.; Wolfe, T.A.; Klein, A.; Studley, N.; Trasorras, J.L. Sintering of WC-12%Co processed by binder jet 3D printing (BJ3DP) technology. *Int. J. Refract. Met. Hard Mater.* **2018**, *71*, 28–35, doi:10.1016/j.ijrmhm.2017.10.023.
37. Enneti, R.K.; Prough, K.C. Wear properties of sintered WC-12%Co processed via Binder Jet 3D Printing (BJ3DP). *Int. J. Refract. Met. Hard Mater.* **2019**, *78*, 228–232, doi:10.1016/j.ijrmhm.2018.10.003.
38. Enneti, R.K.; Prough, K.C. Effect of binder saturation and powder layer thickness on the green strength of the binder jet 3D printing (BJ3DP) WC-12%Co powders. *Int. J. Refract. Met. Hard Mater.* **2019**, *84*, 104991, doi:10.1016/j.ijrmhm.2019.104991.
39. Cramer, C.L.; Wieber, N.R.; Aguirre, T.G.; Lowden, R.A.; Elliott, A.M. Shape retention and infiltration height in complex WC-Co parts made via binder jet of WC with subsequent Co melt infiltration. *Addit. Manuf.* **2019**, *29*, 100828, doi:10.1016/j.addma.2019.100828.
40. Cramer, C.L.; Preston, A.D.; Ma, K.; Nandwana, P. In-situ metal binder-phase formation to make WC-FeNi Cermets with spark plasma sintering from WC, Fe, Ni, and carbon powders. *Int. J. Refract. Met. Hard Mater.* **2020**, *88*, 105204, doi:10.1016/j.ijrmhm.2020.105204.
41. Cramer, C.L.; Nandwana, P.; Lowden, R.A.; Elliott, A.M. Infiltration studies of additive manufacture of WC with Co using binder jetting and pressureless melt method. *Addit. Manuf.* **2019**, *28*, 333–343, doi:10.1016/j.addma.2019.04.009.
42. Schneider, C.A.; Rasband, W.S.; Eliceiri, K.W. NIH Image to ImageJ: 25 years of image analysis. *Nat. Methods* **2012**, *9*, 671–675, doi:10.1038/nmeth.2089.
43. Prakash, L. Fundamentals and General Applications of Hardmetals. In *Comprehensive Hard Materials*; Elsevier, 2014; Vol. 1, pp. 29–90 ISBN 9780080965284.
44. Fang, Z.Z. Correlation of transverse rupture strength of WC–Co with hardness. *Int. J. Refract. Met. Hard Mater.* **2005**, *23*, 119–127, doi:10.1016/j.ijrmhm.2004.11.005.
45. Xiong, H.; Li, Z.; Zhou, K. TiC whisker reinforced ultra-fine TiC-based cermets: Microstructure and mechanical properties. *Ceram. Int.* **2016**, *42*, 6858–6867, doi:10.1016/j.ceramint.2016.01.069.